

# Two-Phase Lorentz Coils and Linear Halbach Array for Multiaxis Precision-Positioning Stages With Magnetic Levitation

Vu Huy Nguyen<sup>1</sup>, Member, IEEE, and Won-jong Kim<sup>2</sup>, Senior Member, IEEE

**Abstract**—In this paper, a new framework for linear permanent-magnet (PM) machines with applications in precision motion control is proposed and validated. A single forcer generating two independent force components in two perpendicular directions is the fundamental unit of the framework. Each forcer consists of two planar Lorentz coils separated by a 90° or 270° phase difference and parallel to a Halbach magnet array. Many coil pairs can be assembled to the same platen to move over a common magnet matrix, forming a linear or planar PM motor. Advantages of this framework include a linear system model, the capability to magnetically levitate the mover in multiaxis stages, and that to generate long translational motion range. The framework developed herein is validated by a six-degree-of-freedom magnetically levitated (maglev) stage. The dimension of the moving platen's frame is 14.3 cm × 14.3 cm, and its total mass is 0.75 kg. The achieved positioning resolution in translations along  $X$ ,  $Y$ , and  $Z$  is 10 nm. The positioning resolution in out-of-plane rotation is 0.1  $\mu$ rad, which is a record in the literature. The maximum travel range in  $XY$  with laser interferometers is 56 mm × 35 mm, limited by the size of the precision mirrors. With the coils' total mass of only 0.205 kg, the achieved acceleration is 1.2 m/s<sup>2</sup>. Experimental results exhibit reduced perturbations in other axes of in-plane motions.

**Index Terms**—Interferometer stages, magnetic levitation, nanopositioning, permanent-magnet (PM) linear motors.

## I. INTRODUCTION

LINEAR motors have been widely used for decades in machine tools, scientific instruments, stepping and scanning devices, and robotics. Linear motors with a maglev mover have no backlash and rotation-induced vibrations compared to conventional ones with rotary motors and lead screws. Maglev mo-

tors can avoid wear, friction loss, use of lubricants, and wear particles generated during motions in the case of direct-driven linear motors with mechanical bearings.

Maglev multiaxis positioners were developed to have travel ranges of centimeters in the  $xy$  plane with a nanoscale positioning resolution [1], [2]. For planar maglev stages with a magnet matrix and a Lorentz coil array, the translational travel range is the difference between the sizes of the magnet matrix and the coil array. The ratio between the maximum travel range and the length of the structure can be considerably larger than that of flexure-based stages. In [2], this ratio is 5.24/10 compared to 1/10 in a flexure design [3]. Maglev linear motors and multi-axis stages are highly applicable in the systems that strictly require high positioning precision, long travel ranges, vibration isolation, and conditions for clean room operations.

The magnetic bearings in linear motors and multi-axis stages may have moving coils [2], moving magnets [1], [4], [5]–[8], or both coils and magnets fixed to the moving platen [8], iron core [6], [8], or air core [1], [2], [5]. For force generation, there are forces produced by the induced currents in short-circuit superconducting tracks [9], zero-field-cooled superconductors [10], electrostatics [11], electromagnets [8], Lorentz coils [1], [2], [5], [6], and Lorentz coils combined with permanent magnets on both the mover and the stator [12].

Trumper *et al.* introduced the use of linear Halbach magnet arrays for magnetic levitation [13]. In this configuration, a forcer has a linear Halbach magnet array on top of 3-phase air-core stator coils. Three phases of coil windings cover exactly half of a spatial pitch of the Halbach array. The normal Lorentz force is to levitate the moving magnets. Kim developed a nanoprecision six-degree-of-freedom (6-DOF) maglev planar motor [1]. Hu and Kim later developed a 6-axis maglev stage with the same framework but the coils were moving atop a stationary Halbach magnet matrix [2]. Zhang and Menq presented a 6-axis maglev stage actuated by three 2-axis Lorentz-force linear actuators [4]. Its travel range was 2 mm × 2 mm × 2 mm in translations and 4° × 4° × 4° in rotations. This 2-axis linear-actuator design allowed for a few degrees of rotation of the mover without significant error in the force model.

In the family of the maglev positioning stages with 6-DOF motions, nanoscale positioning resolution, and centimeter-order travel ranges, there have been only a few designs reported [1], [2], [14]. This paper is to propose and test a 2-phase Lorentz-coil structure that can allow for the design of a 6-DOF maglev stage

Manuscript received September 27, 2016; revised January 2, 2017 and May 18, 2017; accepted September 18, 2017. Date of publication November 1, 2017; date of current version December 13, 2017. This work was supported in part by a grant from the Vietnam Education Foundation (VEF). The opinions, findings, and conclusions stated herein are those of the authors and do not necessarily reflect those of VEF. Recommended by Technical Editor Z. Sun. (Corresponding author: Vu Huy Nguyen.)

V. H. Nguyen is with the Department of Industrial and Systems Engineering, Texas A&M University, College Station, TX 77843 USA (e-mail: vhn1182@gmail.com).

W.-J. Kim is with the Department of Mechanical Engineering, Texas A&M University, College Station, TX 77843 USA (e-mail: wjkim@tamu.edu).

Color versions of one or more of the figures in this paper are available online at <http://ieeexplore.ieee.org>.

Digital Object Identifier 10.1109/TMECH.2017.2769160

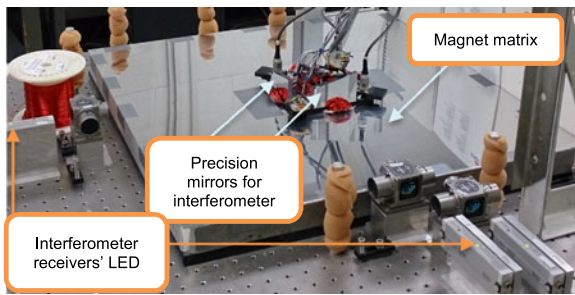


Fig. 1. Setup of the 6-axis maglev stage developed in this work.

added to that family. With a simple mechanical design, mathematical model and linear controller, the achieved positioning resolution in  $XY$  of the 6-DOF maglev stage developed herein is 10 nm compared to 20 nm in [2], 3-nm root-mean-square (rms) positioning noise compared to tens of nanometers in [14]. In out-of-plane rotation, the stage presented in this paper can achieve a record positioning resolution of  $0.1 \mu\text{rad}$ . Compared to other maglev stages reported in [15], [16], which offered a positioning resolution only in the order of micrometers, the control performance in this work is more advantageous in both settling time and reduced perturbations.

To improve the nanopositioning performance, the number of coils to be energized in each design is a factor that must be considered. However, this has not been discussed in most of the previous works. A greater number of coils lead to larger error forces and torques added to the electromechanical system. The sources of error include the geometrical defects of the coils and their mounts. The imperfect perpendicularity and parallelism between coil sides and motor axes are another source of error. In addition, a greater number of coils lead to a higher number of power amplifiers required to energize the stage, and larger uncertainty due to the variations in coils' resistance, inductance, and fill factor. These errors and uncertainties absolutely affect the accuracy of the system's mathematical model and the power-electronic calibration. The number of coils used in [2], [14], and [17] were at least 1.5 times larger than that of the stage developed herein.

In our conference paper [18], the theoretical framework of two Lorentz coils and a linear Halbach array forming a forcer and generating two independent force components was derived. The mechanical design of a maglev stage was reported. However, the stage's position was measured by Hall-effect sensors with a  $6\text{-}\mu\text{m}$  rms noise. Nanopositioning was not demonstrated. The force calculation and the stage's mathematical model were not verified to be sufficiently accurate for nanoscale motions. Control system design was not discussed in detail. In the work presented herein, laser interferometers are used for in-plane position sensing. The stage's nanopositioning capability is validated. Parameter identification is employed to quantify the effects of the force disturbance from the wires connected to the platen and the dc control effort that levitates it. Controller design is discussed, and experimental results include positioning resolution, motion trajectories, and maximum speed and acceleration. Fig. 1 is a photograph of the 6-DOF maglev stage.

This paper is significantly different from our previous work presented in [19], [20], where the stage could only perform 3-DOF motions in micrometer-scale precision. In this work, a

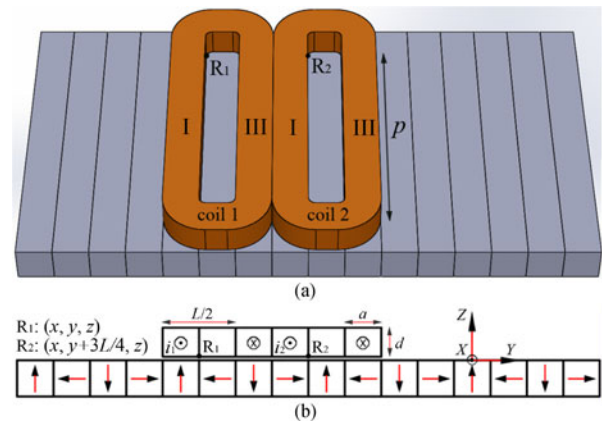


Fig. 2. (a) 3-D model of the forcer with two planar coils and the linear Halbach array and (b) the coil sides and magnets' cross-sectional view.

6-axis stage with eight Lorentz coils arranged in a cross configuration are built and tested. The motivation behind the selection of this cross configuration having eight coils divided into four sets, each with two phases, is to decouple the motions in all the axes. This could not be achieved by the 6-coil structure arranged in a triangle as in [19], [20].

In [2], the planar coils were placed vertically, and only the bottom side of each rectangular coil (the closest to the magnet matrix) was effective for force generation. Three other sides were wasted and added more mass to the moving part. In this paper, the planar coils are laid down and placed horizontally. Two longer sides of each coil are effective for force generation. In case the coil sides and the magnets depicted in Fig. 2 have the same width in  $Y$ , the two coils cover a length of  $1.5L$ . Here,  $L$  is the spatial pitch of the linear Halbach array, corresponding to four magnet bars. Nine coils were needed for the same length in [2]. With the same maximum currents, coil thickness, and coil length, the peak force produced by this 2-phase forcer is  $2/3$  that of the 3-phase 9-coil forcer. The total coil volume of the 2-phase forcer is only  $1/3$  that of the 3-phase one. Hence, the power density of the 2-phase forcer is approximately twice that of the 3-phase one.

A key feature that makes the nanoscale motion of the stage ultraquiet is the overlapped Lorentz coils. The coils are overlapped firstly to further reduce the area that they cover on the frame of the moving platen. The total area and the mass of the moving platen can, therefore, be reduced. Second, the overlapped coils help reduce the variance of the equivalent vertical forces' acting points by a factor of 2 compared to that of separated coils, as depicted in Fig. 5(b). The coupling effects among different control axes are, therefore, reduced due to smaller out-of-plane error torques. This is the first time overlapped Lorentz coils are demonstrated in maglev nanopositioning. Another key feature of this paper is that the parameter identification method discussed herein has not been attempted in the literature of maglev positioning. None of the prior art discussed the design and control to decouple all the axes by a minimum number of coils, and how to reduce perturbations by the mechanical design and force allocation, and the selection of control bandwidths for the control axes.

Section II of this paper discusses our theoretical framework and the Lorentz force calculation. Section III presents the newly developed 6-axis maglev stage. Mechanical dynamics of the stage is presented in Section IV. Section V shows experimental results and discussions to validate the theoretical framework. Section VI gives the conclusions.

## II. FRAMEWORK WITH 2-PHASE LORENTZ COILS AND A LINEAR HALBACH ARRAY

### A. Theoretical Framework

The moving-coil design is selected in this paper due to two main reasons. First, the planar coil's shorter sides ineffective for force generation can be bent and placed farther away from the top surface of the magnet array. This minimizes the coils' end effects. The force calculation is, therefore, more precise and greatly simplified. Second, the magnetic field generated by the stationary magnet matrix can be measured to give the moving platen's in-plane positions. This helps initialize the platen's position to be well aligned with the laser beams for nanoresolution position sensing. Fig. 2(a) is a three-dimensional (3-D) model of the forcer developed herein. The two coils are separated by a 270° phase difference. The cross-sectional view of the coils and the Halbach array is depicted in Fig. 2(b).

On a plane close and parallel to the top surface of the magnet array depicted in Fig. 2(b), the  $z$ -direction and  $y$ -direction flux density components are sinusoidally dependent on the  $y$ -axis position. The period of this variation is one spatial pitch of the magnet array,  $L$ . The planar coils that constitute a forcer are designed so that two effective sides of each coil are separated by  $L/2$ . The magnetic-field components and the electric currents in the two coil sides are equal in magnitude but opposite in direction. The Lorentz forces at the two sides add up to be twice that of each side. Two coils are required to produce two orthogonal and independent force components. From the force calculation of a single side, one can directly determine the total Lorentz force of all four sides of the 2-coil forcer.

### B. Magnetic Field of the Linear Halbach Array

In the space surrounding a linear Halbach array, the flux lines are focused on one side. The magnetic flux density on that side is  $\sqrt{2}$  times stronger than that of a conventional magnet array [13]. The Halbach array is applicable in linear permanent-magnet machines, where a precise and linear force model and high force density are needed. Fig. 2(b) depicts a linear Halbach array with 16 magnet pieces. The magnet array's strong side is in the positive  $z$ -direction. Above the array's top surface, the magnetic field has two components in the  $y$ - and  $z$ -directions. Assuming that the magnet array is infinitely long in the  $y$ -direction, the field solution was presented in [1], [13]. The  $y$ - and  $z$ -direction flux-density components at the point  $(y, z)$  over the array's top

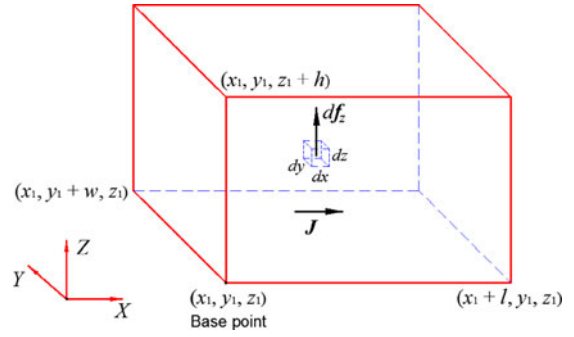


Fig. 3. Right-rectangular-prism coil side for the derivation of volume integration in the force calculation.

surface are

$$B_y(y, z) = \sum_{k=0}^{+\infty} (-1)^k c_n(z) \sin(\gamma_n y) \quad (1)$$

$$B_z(y, z) = \sum_{k=0}^{+\infty} (-1)^k c_n(z) \cos(\gamma_n y) \quad (2)$$

where

$$c_n(z) = \frac{2\sqrt{2}\mu_0 M_0}{\pi n} (1 - e^{-\gamma_n \Delta}) e^{-\gamma_n z}. \quad (3)$$

In (1)–(3),  $n = 4k + 1$ ,  $\mu_0$  is the permeability of free space,  $M_0$  is the permanent magnets' peak magnetization,  $\gamma_n = 2\pi n/L$ , and  $\Delta$  is the magnet array's thickness in the  $z$ -axis.

### C. Lorentz Forces Generated by a Right-Rectangular-Prism Coil Volume

The calculation of the horizontal Lorentz-force components in the  $XY$  plane was presented in [18], [19]. The calculation of the normal force in the vertical axis is presented in this paper with the use of the current density instead of the electric current as in [18], [19]. To establish the current-force relation for a forcer with two coils placed over a linear Halbach array, a right-rectangular-prism coil side, as in Fig. 3, is considered.

All the segments of the winding in the right-rectangular-prism volume of each coil side are assumed to be straight. For the two longer sides of each coil in Fig. 2(a), the transverse Lorentz force is generated by the  $z$ -axis flux density,  $B_z(y, z)$ . The normal Lorentz force is generated by the  $y$ -axis magnetic-flux density,  $B_y(y, z)$ . Volume integration is performed to calculate these Lorentz forces. The reference point from which the integration is taken is  $(x_1, y_1, z_1)$ , as noted in Fig. 3.

The Lorentz force  $f_z$  generated by the  $y$ -axis flux density in (1) is calculated. The amount of Lorentz force generated by an incremental volume of  $dx dy dz$  of the coil side is

$$d\mathbf{f}_z = (J dy dz dx \mathbf{i}_x) \times (B_y \mathbf{i}_y) = J B_y dy dz dx \mathbf{i}_z \quad (4)$$

where  $J$  ( $A/m^2$ ) is the current density flowing along the  $x$ -direction in the coil side. The unit vectors in the  $x$ -,  $y$ -, and  $z$ -axes are  $\mathbf{i}_x$ ,  $\mathbf{i}_y$ , and  $\mathbf{i}_z$ , respectively. The  $z$ -direction Lorentz force acting on a right-rectangular-prism coil volume with the reference point of  $(x_1, y_1, z_1)$  and dimensions of  $l$  in  $x$ ,  $w$  in  $y$ ,

and  $h$  in  $z$ , is

$$\begin{aligned} f_{lwh,z} &= J \int_{lwh} B_y dx dy dz \\ &= J \int_{z_1}^{z_1+h} \int_{y_1}^{y_1+w} \sum_{k=0}^{+\infty} q_n(z) \sin(\gamma_n y) \left( \int_{x_1}^{x_1+l} dx \right) dy dz \end{aligned} \quad (5)$$

where

$$q_n(z) = (-1)^k c_n(z) = \frac{(-1)^k 2\sqrt{2}\mu_0 M_0}{\pi n} (1 - e^{-\gamma_n \Delta}) e^{-\gamma_n z}.$$

Using

$$\int_{z_1}^{z_1+h} \frac{q_n(z)}{\gamma_n} dz = \frac{1}{\gamma_n^2} q_n(z_1) (1 - e^{-\gamma_n h})$$

we have

$$\begin{aligned} f_{lwh,z} &= J l \sum_{k=0}^{+\infty} \frac{2}{\gamma_n^2} q_n(z_1) \sin \left[ \gamma_n \left( y_1 + \frac{w}{2} \right) \right] \\ &\quad \times \sin \left( \frac{\gamma_n w}{2} \right) (1 - e^{-\gamma_n h}). \end{aligned} \quad (6)$$

For the calculation of the  $y$ -direction force generated by the same right-rectangular prism, one can refer to [19]

$$\begin{aligned} f_{lwh,y} &= -J l \sum_{k=0}^{+\infty} \frac{2}{\gamma_n^2} q_n(z_1) \cos \left[ \gamma_n \left( y_1 + \frac{w}{2} \right) \right] \\ &\quad \times \sin \left( \frac{\gamma_n w}{2} \right) (1 - e^{-\gamma_n h}). \end{aligned} \quad (7)$$

#### D. Lorentz Forces Generated by a Rectangular Coil

Provided that the dimension of the magnet array in the  $x$ -axis is larger than that of the coil side, neglecting the effects of the coil corners, the two shorter coil sides as seen in Fig. 2(a) only produce the  $x$ -direction force component. The electric currents in the two shorter sides have equal magnitude and opposite directions. Therefore, the two Lorentz forces in  $x$  generated by the shorter sides cancel. For the calculation of the Lorentz forces in  $y$ - and  $z$ -directions generated by coil 1, the coil's reference point for volume integration is  $(x, y, z)$ , as in Fig. 2(b). The distance between the coil's bottom surface and the Halbach array's top surface is  $z$ .

The base points to calculate the Lorentz forces acting on the right-rectangular-prism volumes I and III of coil 1 are  $(x, y - a, z)$  and  $(x, y - a + L/2, z)$ , respectively. From the force calculation in Section II-C, the Lorentz forces in the  $y$ - and  $z$ -axes generated by coil 1 are given below:

$$\begin{aligned} f_{\text{coil},z} &= J_1 p \sum_{k=0}^{+\infty} \frac{4}{\gamma_n^2} q_n(z) \sin \left[ \gamma_n \left( y - \frac{a}{2} \right) \right] \\ &\quad \times \sin \left( \frac{\gamma_n a}{2} \right) (1 - e^{-\gamma_n d}) \end{aligned} \quad (8)$$

$$\begin{aligned} f_{\text{coil},y} &= -J_1 p \sum_{k=0}^{+\infty} \frac{4}{\gamma_n^2} q_n(z) \cos \left[ \gamma_n \left( y - \frac{a}{2} \right) \right] \\ &\quad \times \sin \left( \frac{\gamma_n a}{2} \right) (1 - e^{-\gamma_n d}). \end{aligned} \quad (9)$$

It is assumed that the coil's position in the vertical axis is not changed in 6-axis closed-loop control. When the coil moves along the  $y$ -axis, the amplitudes of the force components in (8) and (9) associated with the higher harmonics are negligible compared with that of  $n = 1$ . For example, with  $\Delta = 12.7$  mm,  $z = 2$  mm,  $p = 42.29$  mm,  $a = 9.65$  mm, and  $d = 2.54$  mm, the force amplitudes of the 5th and 9th harmonics are only 0.3% and 0.1% that of the fundamental harmonics, respectively. For linear controller design and real-time implementation, the simplified force expressions are

$$f_{\text{coil},z} = J_1 p \frac{4}{\gamma_1^2} c_1(z) \sin \left[ \gamma_1 \left( y - \frac{a}{2} \right) \right] \sin \left( \frac{\gamma_1 a}{2} \right) (1 - e^{-\gamma_1 d}) \quad (10)$$

$$f_{\text{coil},y} = -J_1 p \frac{4}{\gamma_1^2} c_1(z) \cos \left[ \gamma_1 \left( y - \frac{a}{2} \right) \right] \sin \left( \frac{\gamma_1 a}{2} \right) (1 - e^{-\gamma_1 d}). \quad (11)$$

#### E. Lorentz Forces Generated by a 2-Coil Forcer With 270° or 90° Phase Difference

In Fig. 2, the forcer's two coils are placed at a distance of  $3L/4$  in the  $y$ -axis. They have a 270° phase difference. The Lorentz forces generated by coil 2 in the  $z$ - and  $y$ -axes are derived by substituting  $y + 3L/4$  for  $y$  and  $J_2$  for  $J_1$  in (10) and (11). Here,  $J_2$  is coil 2's current density. The resultant forces generated by the forcer with two coils are

$$F_{12,z} = b_1(z) \left\{ J_1 \sin \left[ \gamma_1 \left( y - \frac{a}{2} \right) \right] - J_2 \cos \left[ \gamma_1 \left( y - \frac{a}{2} \right) \right] \right\} \quad (12)$$

$$F_{12,y} = b_1(z) \left\{ -J_1 \cos \left[ \gamma_1 \left( y - \frac{a}{2} \right) \right] - J_2 \sin \left[ \gamma_1 \left( y - \frac{a}{2} \right) \right] \right\} \quad (13)$$

where

$$b_1(z) = p c_1(z) \frac{4}{\gamma_1^2} \sin \left( \frac{\gamma_1 a}{2} \right) (1 - e^{-\gamma_1 d}).$$

In case the forcer's two coils are overlapped and placed at a distance of  $L/4$  in the  $y$ -direction, their phase difference is 90°. The reference points of coils 1 and 2 are  $(x, y, z)$  and  $(x, y + L/4, z)$ , respectively. The Lorentz forces generated by coil 2 are determined by substituting  $y + L/4$  for  $y$  and the current density  $J_2$  for  $J_1$  in (10) and (11). The forces in the  $z$ - and  $y$ -axes generated by the forcer are, respectively,

$$F_{12,z} = b_1(z) \left\{ J_1 \sin \left[ \gamma_1 \left( y - \frac{a}{2} \right) \right] + J_2 \cos \left[ \gamma_1 \left( y - \frac{a}{2} \right) \right] \right\} \quad (14)$$

$$F_{12,y} = b_1(z) \left\{ -J_1 \cos \left[ \gamma_1 \left( y - \frac{a}{2} \right) \right] + J_2 \sin \left[ \gamma_1 \left( y - \frac{a}{2} \right) \right] \right\}. \quad (15)$$

For a planar stage with the distance between the magnet array and the coils varying in a small range,  $b_1(z)$  in (12)–(15) can be evaluated at the nominal air gap. The linear force-current transformation, therefore, depends only on the platen's position in the  $y$ -direction. The platen's position in  $z$  can still be controlled precisely by a closed-loop controller. This is validated with experimental results in Section V.

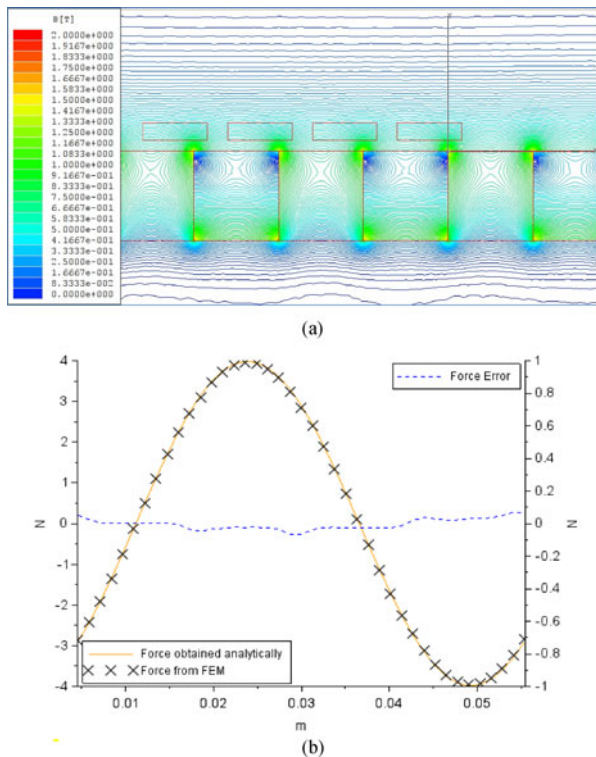


Fig. 4. (a) FEM image of the magnetic flux density and (b) plots of the force from FEM compared with that of analytical calculation.

### F. Finite-Element-Method (FEM) Verification of the Force Calculation

A 2-D FEM is applied to verify the correctness and accuracy of the force calculation presented above. In the case considered here, the Lorentz forces in  $y$  and  $z$  generated by a forcer are obtained from an FEM and the analytical solution derived in Section II-E. The forcer has two overlapped coils with a  $90^\circ$  phase difference. The geometrical parameters as in Fig. 2 are  $\Delta = 12.7$  mm,  $z = 2$  mm,  $p = 42.29$  mm,  $a = 9.65$  mm, and  $d = 2.54$  mm. The two-coil forcer considered herein is different from the one in Fig. 2 only in the distance between the two coils,  $L/4$  instead of  $3L/4$ . The permanent magnets are NdFeB 35. The current densities in the coils are  $J_1 = J_2 = 4 \times 10^6$  A/m<sup>2</sup>. Fig. 4(a) shows the magnetic flux density obtained from the FEM at a certain position of the coils above the magnet array. In Fig. 4(b), the  $y$ -direction Lorentz forces obtained analytically and by an FEM are plotted in a spatial pitch in  $y$  of the magnet array. The error between the results from the FEM and the analytical solution is within 1% of the peak-to-peak force amplitude.

### III. NEWLY CONSTRUCTED 6-AXIS MAGLEV STAGE

With two orthogonal and independent forces produced by a forcer, multiple forcers can be grouped to form a linear motor or a multi-DOF stage. Many coil pairs can be fixed to a common platen moving over the same magnet array. To have a symmetric configuration in  $x$  and  $y$ , four forcers are utilized for the 6-axis

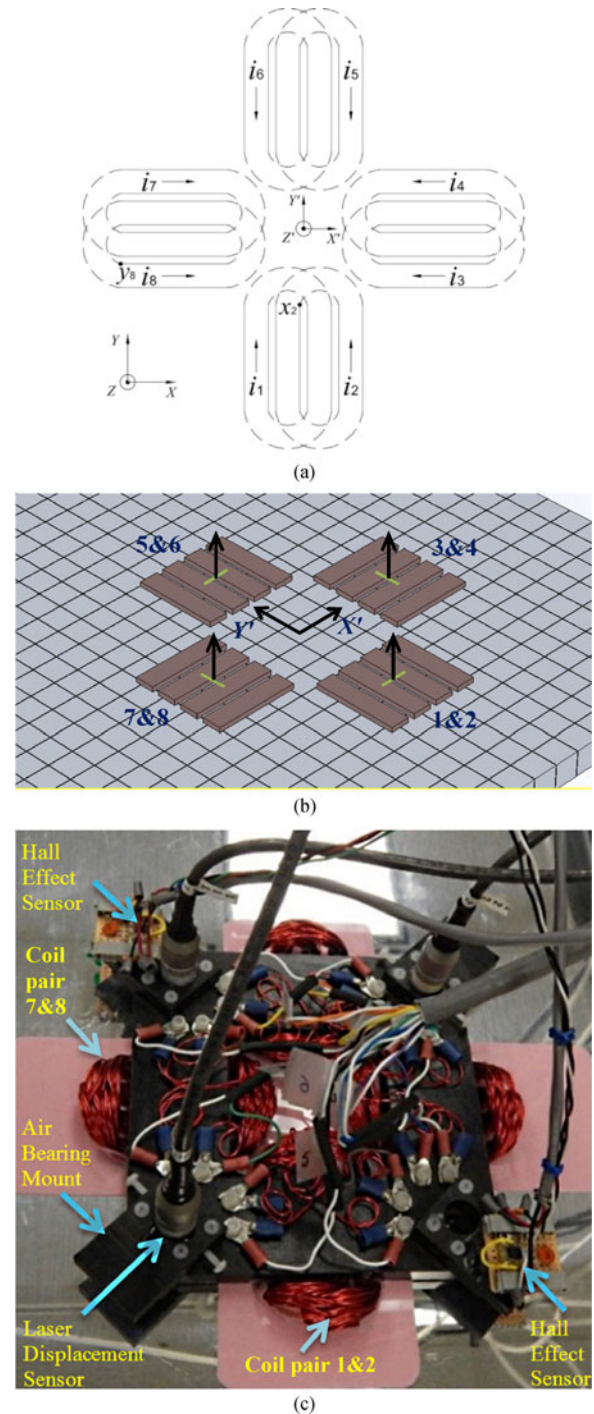


Fig. 5. (a) Illustration of the four coil pairs, (b) the vertical forces generated by the four forcers, and (c) a photograph of the platen.

stage in this paper. Fig. 5(a) depicts the eight overlapped coils in the platen.

The decoupled dynamics is realized thanks to two features of the design. First, the forces in each axis,  $x$  and  $y$ , can be generated independently by a set of only two opposite forcers, 1&2 and 5&6, and 3&4 and 7&8, respectively, which could not be possible in [2], [18], [19]. The torque about each in-plane axis,  $X'$ - and  $Y'$ , can be independently produced by a set of only

two forcers, 1&2 and 5&6, and 3&4 and 7&8, respectively. To generate a force or a torque, a greater number of forcers lead to larger error forces and torques added to the system. These errors can originate from the geometrical defects of the structure with the motor axes not perfectly perpendicular or parallel, coupling between forces generated by different motors, and additional errors due to the variations in the coils' resistance and inductance.

The acting point of the resultant vertical force generated by two overlapped coils, 5&6, for example, only stays in the narrow space between the two adjacent sides close to the  $Y'$ -axis, as illustrated in Fig. 5(b). The torque about the  $Y'$ -axis due to this force can be neglected to greatly simplify the system model. Only the vertical forces by the coil pairs 3&4 and 7&8 are counted in the calculation of the torque about  $Y'$ .

Fig. 5(c) shows the platen with its components. Each coil side has  $N = 30$  turns stacked in three layers. Its thickness, width, and the effective length for force generation are  $d = 2.54$  mm,  $a = 9.65$  mm, and  $p = 42.29$  mm, respectively. The four sides of two overlapped coils are equally separated by  $L/4$ , which is 12.7 mm. Each coil has the resistance of  $0.19 \Omega$  and the inductance of  $59 \mu\text{H}$ . The mass of each pair of two overlapped coils is 51.3 g.

In the platen, there are a plastic frame, four pairs of overlapped coils, four sensor mounts, three vertical laser displacement sensors, two Hall-effect sensors, as shown in Fig. 5(c), and two precision mirrors, as seen in Fig. 1. Delrin Acetal resin, a material with high tensile strength (62–73 MPa) and low density ( $1.4 \text{ g/cm}^3$ ) is used to make the platen's frame and the sensor mounts. In Fig. 5(c), the parts fixed to the frame's corners house the vertical laser sensors and support the air bearings (needed for initial testing). A laser head (HP 5517D) and three interferometers (HP 10706B) manufactured by Agilent Technologies are used to measure the platen's positions in  $x$ ,  $y$ , and  $\theta_z$ . The dimensions of the frame are  $143 \text{ mm} \times 143 \text{ mm}$ . The total height of the frame and sensor mounts without the vertical laser sensors is 18.03 mm. The total mass of the platen is  $m = 0.75 \text{ kg}$ . Its moments of inertia about the  $X'$ -,  $Y'$ -, and  $Z'$ -axes are  $I_x = I_y = 0.0019 \text{ kg} \cdot \text{m}^2$ , and  $I_z = 0.0036 \text{ kg} \cdot \text{m}^2$ , respectively.

#### IV. SYSTEM DYNAMICS OF THE 6-DOF MAGLEV STAGE

For this stage, the travel range of the platen is  $40 \mu\text{m}$  in  $z$  while the distance between the magnets' top surface and the coils' bottom surface is 1.6 mm. The rotations about the horizontal axes are within  $1 \mu\text{rad}$ . The force model was derived with the assumptions that the  $Z$ -axis position in the force calculation is fixed at 1.6 mm and the coil sides are aligned with the  $X$ - or  $Y$ -axis. With this, the system model derived herein is linear. With the platen considered a pure mass, the system dynamics is based on Newton's second law

$$m\ddot{x} = F_x, m\ddot{y} = F_y, I_z\ddot{\theta}_z = T_z \quad (16)$$

$$m\ddot{z} = F_z, I_x\ddot{\theta}_x = T_x, I_y\ddot{\theta}_y = T_y. \quad (17)$$

The platen's positions in the  $X$ -,  $Y$ -, and  $Z$ -axes are  $x$ ,  $y$ , and  $z$ , and its rotation angles about the  $X'$ -,  $Y'$ -, and  $Z'$ -axes are  $\theta_x$ ,  $\theta_y$ , and  $\theta_z$ , respectively. The  $XYZ$  and  $X'Y'Z'$  frames in Fig. 5(a) are fixed to the magnet matrix and the moving platen,

respectively.  $F_x$ ,  $F_y$ , and  $F_z$  are the total forces generated by all the forcers in the  $X$ -,  $Y$ -, and  $Z$ -axes.  $T_x$ ,  $T_y$ , and  $T_z$  are the total torques acting on the platen about the  $X'$ -,  $Y'$ -, and  $Z'$ -axes, respectively, generated by the Lorentz forces at the forcers. In targeted applications, the platen's position in  $z$  is controlled only to track a constant reference. To levitate the platen from rest to a certain height, the control effort in  $z$  is increased by repeatedly feedforwarding a constant amount. This is done while the control loops in  $x$ ,  $y$ , and  $\theta_z$  are closed. After that the loop in  $z$  is closed. Therefore, in (17), the platen's weight is omitted. It is eventually canceled by the dc control effort.

The transformation between the total forces and torques acting on the platen and the forcers' Lorentz forces is

$$\begin{bmatrix} F_x \\ F_y \\ T_z \\ F_z \\ T_x \\ T_y \end{bmatrix} = \begin{bmatrix} 1 & 0 & 0 & 0 & 1 & 0 & 0 & 0 \\ 0 & 0 & 1 & 0 & 0 & 0 & 1 & 0 \\ l & 0 & l & 0 & -l & 0 & -l & 0 \\ 0 & 1 & 0 & 1 & 0 & 1 & 0 & 1 \\ 0 & -l & 0 & 0 & 0 & l & 0 & 0 \\ 0 & 0 & 0 & -l & 0 & 0 & 0 & l \end{bmatrix} \begin{bmatrix} F_{12,x} \\ F_{12,z} \\ F_{34,y} \\ F_{34,z} \\ F_{56,x} \\ F_{56,z} \\ F_{78,y} \\ F_{78,z} \end{bmatrix} \quad (18)$$

$$= A \begin{bmatrix} F_{12,x} \\ F_{12,z} \\ F_{34,y} \\ F_{34,z} \\ F_{56,x} \\ F_{56,z} \\ F_{78,y} \\ F_{78,z} \end{bmatrix}.$$

In the  $6 \times 8$  matrix of  $A$ ,  $l = 0.05207 \text{ m}$  is the distance from the midpoint of each coil side to the platen's symmetric axis perpendicular to that side. The relation between the electric currents and the eight Lorentz forces generated by the forcers is

$$\begin{bmatrix} F_{12,x} & F_{12,z} & F_{34,y} & F_{34,z} & F_{56,x} & F_{56,z} & F_{78,y} & F_{78,z} \end{bmatrix}^T = b_*(z) \begin{bmatrix} sx & -cx & 0 & 0 & 0 & 0 & 0 & 0 \\ cx & sx & 0 & 0 & 0 & 0 & 0 & 0 \\ 0 & 0 & cy & sy & 0 & 0 & 0 & 0 \\ 0 & 0 & -sy & cy & 0 & 0 & 0 & 0 \\ 0 & 0 & 0 & 0 & cx & -sx & 0 & 0 \\ 0 & 0 & 0 & 0 & -sx & -cx & 0 & 0 \\ 0 & 0 & 0 & 0 & 0 & 0 & -sy & -cy \\ 0 & 0 & 0 & 0 & 0 & 0 & -cy & sy \end{bmatrix} \begin{bmatrix} i_1 \\ i_2 \\ i_3 \\ i_4 \\ i_5 \\ i_6 \\ i_7 \\ i_8 \end{bmatrix} \quad (19)$$

where  $sx = \sin(\gamma_1 x_2)$ ,  $cx = \cos(\gamma_1 x_2)$ ,  $sy = \sin(\gamma_1 y_8)$ , and  $cy = \cos(\gamma_1 y_8)$ . The positions of the base points,  $x_2$  and  $y_8$  are shown in Fig. 5(a). The electric current in the  $j$ th coil is  $i_j$

$$b_*(z) = \frac{N}{da} b_1(z) = pc_1(z) \frac{4N}{da\gamma_1^2} \sin\left(\frac{\gamma_1 a}{2}\right) (1 - e^{-\gamma_1 d}) \quad (20)$$

where  $c_1(z)$  is evaluated at the nominal gap of  $z_0 = 0.0016 \text{ m}$ .

From (18), to have a linear transformation between the total forces and torques acting on the platen and the control efforts  $u_x, u_y, u_{\theta_z}, u_z, u_{\theta_x},$  and  $u_{\theta_y}$ , the pseudoinverse of the matrix  $A$  is calculated to be  $B$  and used as follows:

$$\begin{bmatrix} F_{12,x} & F_{12,z} & F_{34,y} & F_{34,z} & F_{56,x} & F_{56,z} & F_{78,y} & F_{78,z} \end{bmatrix}^T = 2Bb_*(z_0)U$$

$$U = [u_x \ u_y \ u_{\theta_z} \ u_z \ u_{\theta_x} \ u_{\theta_y}]^T. \quad (21)$$

With (18) and (21), all six control axes can be decoupled. The linear system model is as below:

$$\begin{bmatrix} m\ddot{x} & m\ddot{y} & I_z\ddot{\theta}_z & m\ddot{z} & I_x\ddot{\theta}_x & I_y\ddot{\theta}_y \end{bmatrix}^T = 2b_*(z_0)U. \quad (22)$$

The transformation between the eight electric currents and the six control efforts is established from (19) and (21)

$$\begin{bmatrix} i_1 & i_2 & i_3 & i_4 & i_5 & i_6 & i_7 & i_8 \end{bmatrix}^T = \frac{1}{b_*(z_0)} \begin{bmatrix} sx & cx & 0 & 0 & 0 & 0 & 0 & 0 \\ -cx & sx & 0 & 0 & 0 & 0 & 0 & 0 \\ 0 & 0 & cy & -sy & 0 & 0 & 0 & 0 \\ 0 & 0 & sy & cy & 0 & 0 & 0 & 0 \\ 0 & 0 & 0 & 0 & cx & -sx & 0 & 0 \\ 0 & 0 & 0 & 0 & -sx & -cx & 0 & 0 \\ 0 & 0 & 0 & 0 & 0 & 0 & -sy & -cy \\ 0 & 0 & 0 & 0 & 0 & 0 & -cy & sy \end{bmatrix} \begin{bmatrix} F_{12,x} \\ F_{12,z} \\ F_{34,y} \\ F_{34,z} \\ F_{56,x} \\ F_{56,z} \\ F_{78,y} \\ F_{78,z} \end{bmatrix}. \quad (23)$$

Substituting the left-hand side of (21) into (23), we have

$$\begin{bmatrix} i_1 & i_2 & i_3 & i_4 & i_5 & i_6 & i_7 & i_8 \end{bmatrix}^T = 2S_{xy} B [u_x \ u_y \ u_{\theta_z} \ u_z \ u_{\theta_x} \ u_{\theta_y}]^T. \quad (24)$$

Here,  $S_{xy}$  is the  $8 \times 8$  matrix in (23).

## V. EXPERIMENTAL VALIDATION

The system model given in (22) allows the system to be decoupled into six linear single-input-single-output subsystems for the six control axes. The transfer functions of the plants to be controlled in  $x, y, \theta_z, z, \theta_x,$  and  $\theta_y$  are as follows:

$$G_{xy}(s) = \frac{2.27}{s^2}, G_{\theta_z}(s) = \frac{473.25}{s^2} \quad (25)$$

$$G_z(s) = \frac{2.27}{s^2}, G_{\theta_x}(s) = \frac{896.68}{s^2}. \quad (26)$$

When the platen is at rest, the distance between the top surface of the magnet matrix and the bottom surface of the coils is already 0.0016 m. This includes the thickness of an epoxy layer and a thin aluminum plate on top of the magnet matrix. A dc control effort is used to stably levitate the moving platen in the vertical axis to a nominal height within  $40 \mu\text{m}$  from rest (while the controllers in  $x, y,$  and  $\theta_z$  are in closed loop). This travel range is significantly smaller than 0.0016 m. Therefore in the force calculation  $z$  is fixed at 0.0016 m and the forces generated by each forcer are dependent only in  $x$  or  $y$ . The dc control effort is to maintain a sufficient stiffness of the platen and to allow for a small closed-loop control bandwidth in  $z$ . This greatly reduces the effect of the sensing noise on the output.

For the in-plane control axes of  $x, y,$  and  $\theta_z$ , because the wires vertically connected to the platen from the ceiling are considerably longer than the platen's travel range in  $xy$ , their effect on the in-plane motions is negligible. For the out-of-plane axes,  $\theta_x, \theta_y,$  and  $z$ , parameter identification needs to be implemented to take into account the effects of the dc control effort and the force disturbances from the wires.

This maglev system is open-loop unstable. To maintain its stability, the control of the stage needs to follow the initiation steps as follows. First, the controllers in the in-plane motions ( $x, y,$  and  $\theta_z$ ) must be in closed loop, being designed and tuned to have negligible steady-state errors, sufficiently small rms positioning noise (5 nm or smaller), and sufficiently large control bandwidth (80 Hz or larger). After the stage's in-plane axes are in closed-loop control, a feedforward control effort is introduced to levitate the stage up to a nominal height (within  $40 \mu\text{m}$  from rest). After the maglev stage is levitated, the steady-state errors in  $x$  and  $y$  are unnoticeable at the nanometer scale. When the feedforward control effort is still effective, closed-loop control with small bandwidth (a few hertz) is introduced in  $z$ . The closed-loop control in  $z$  is to adjust the stage's position precisely within the range of a few micrometers from the nominal position. It is possible to hold the stage stably in magnetic levitation without closed-loop control in the rotation about the horizontal axes ( $\theta_x$  and  $\theta_y$ ). However, to produce stable motions in  $x$  and  $y$  in magnetic levitation, the control loops in  $\theta_x$  and  $\theta_y$  need to be closed to reduce the fluctuations in out-of-plane rotations during motions. The steps listed above are performed within a few seconds. Then, the stage is ready to generate all 6-DOF motions in magnetic levitation.

The following proportional-integral-derivative (PID) controller is implemented for the subsystems in  $x$  and  $y$  with the transfer functions given in (25)

$$C_{xy}(s) = 36000 + 100s + 2400000/s. \quad (27)$$

The phase margin is  $33.2^\circ$ , the crossover frequency is 49.8 Hz, and the closed-loop bandwidth is 87.8 Hz. This control bandwidth is sufficient to reject low-frequency disturbances from the cables and maintain sufficient stiffness in  $x$  and  $y$ . A tradeoff to the high bandwidth is the 13-dB peak of the closed-loop gain at 44.9 Hz. Therefore, for large (1 mm or longer) stepping motions in  $x$  and  $y$ , perturbations in the other axes induce the vibrations back to the  $x$ - and  $y$ -axes. Hence, input shaping is required to reduce the perturbations in all the axes, and a trapezoidal-velocity profile is used in this paper.

The continuous-time PID controller for  $\theta_z$  is designed to be

$$C_{\theta_z}(s) = 300 + s + 24000/s. \quad (28)$$

This control system has the phase margin of  $57.1^\circ$ , crossover frequency of 81.3 Hz, and closed-loop bandwidth of 154.3 Hz. The stage has less vibration when the control bandwidth in  $\theta_z$  is higher than that of  $x$  and  $y$ . The reason is that any perturbations in  $\theta_z$  cause considerable perturbations in  $x$  and  $y$  but a perturbation in  $x$  or  $y$  alone may cause no significant fluctuation in  $\theta_z$ . Therefore, the control system's bandwidth in  $\theta_z$  must be sufficiently high to reject a disturbance before it induces other perturbations in  $x$  and  $y$ .

Parameter identification is performed for the system (when the platen is already levitated by the dc control effort) to quantify the effects of both the dc control effort and the force disturbance from the umbilical wires. From observations based on the empirical data, the dc control effort and the wires not only have the stiffness effect but also the damping effect. Therefore, to better represent the dynamics of the out-of-plane systems, the pure-mass models in  $z$ ,  $\theta_x$ , and  $\theta_y$  are augmented to be mass-spring-damper ones. The new model of the dynamics in  $z$  has the form of

$$G_z(s) = \frac{2b_*(z_0)}{m.s^2 + cs + k} = \frac{1.7037}{0.75s^2 + cs + k}. \quad (29)$$

The spring constant  $k$  is identified empirically. A known dc control effort ( $-0.1$ ,  $0.1$ , or  $0.2$  A) is introduced while the platen is stably lifted up to a certain height within  $40 \mu\text{m}$ . The dc control effort cancels the moving platen's weight and maintains a certain position of the platen in  $z$ . Any displacements of the platen from this equilibrium are caused by the added control effort. From this, the dc gain of the transfer function in (29) is determined, and the spring constant  $k$  is estimated to be  $94600 \text{ N/m}$ . The damping coefficient  $c$  in (29) is identified by the phase lag between the output and the sinusoidal input to the open-loop system. While the platen is magnetically levitated by the dc control effort in open loop, a sinusoidal input in  $z$  is introduced, and the output is recorded. From  $k = 94600 \text{ N/m}$  and the observed phase lag with sinusoidal inputs, the damping coefficient  $c$  is calculated to be  $890 \text{ N}\cdot\text{s/m}$ . The system model in  $z$  identified in the vicinity of the nominal position maintained by the dc control effort is

$$G_z(s) = \frac{1.7037}{0.75s^2 + 890.1s + 94600}. \quad (30)$$

The suspension of the moving platen with the four forcers arranged in a cross configuration can be modeled as four parallel supports, each comprising a spring and a damper. These four supports equally contribute to the total spring constant of  $94600 \text{ N/m}$  and damping coefficient of  $890 \text{ N}\cdot\text{s/m}$ . Therefore, the torsional stiffness and damping coefficient for the out-of-plane rotations,  $\theta_x$  and  $\theta_y$ , are identified from the linear spring constant and linear damping coefficient. These parameters and the plant model in  $\theta_x$  and  $\theta_y$  are as follows:

$$k_{\text{torsional}} = (k/2)l^2 = 128 \text{ N}\cdot\text{m/rad}$$

$$c_{\text{torsional}} = (c/2)l^2 = 1.21 \text{ N}\cdot\text{m}\cdot\text{s/rad}$$

$$G_{\theta_{xy}}(s) = 1.7037/(0.0019s^2 + 1.21s + 128). \quad (31)$$

Here,  $l = 52.1 \text{ mm}$  is half the distance between the two opposite forcers. The closed-loop controllers in  $z$  and  $\theta_{xy}$  are

$$C_z(s) = 40000 + 560000/s \quad (32)$$

$$C_{\theta_{xy}}(s) = 70 + 0.09s + 17600/s. \quad (33)$$

The closed-loop controller in  $z$  is to finely adjust the platen's position within a few micrometers from the nominal position maintained by the dc control effort. This generates certain force stiffness in  $z$  so that, in addition to the dc control effort, only a small closed-loop bandwidth in  $z$  is required. It is  $1.2 \text{ Hz}$  in this

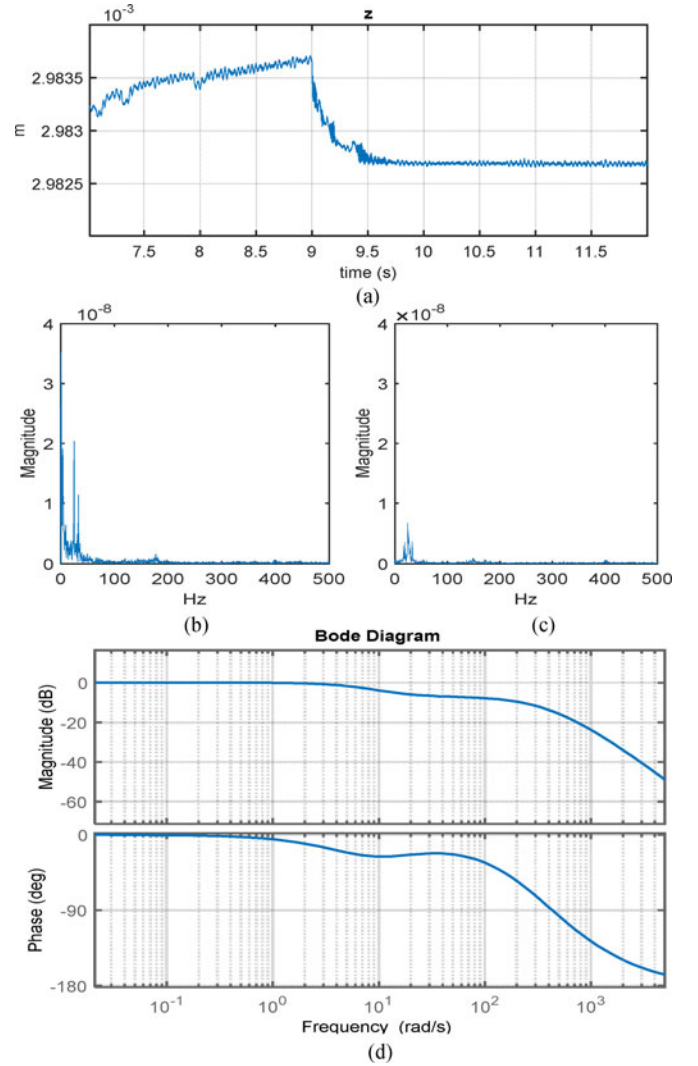


Fig. 6. (a) Plot of the platen's position in  $z$  where it is lifted up by an open-loop control effort before the time of  $9 \text{ s}$ . (b) Fourier transform of the positioning noise shown in (a) between  $7$  and  $9 \text{ s}$ , and (c) Fourier transform of the noise in  $10$ – $12 \text{ s}$ , and (d) Bode plot of the closed-loop system in  $z$ .

case. The sensing noise's effect can, therefore, be minimized. Fig. 6(b) and (c), respectively, shows the frequency spectrum of the positioning noise before and after the closed-loop controller is added at  $9 \text{ s}$ , as can be seen in Fig. 6(a). Fig. 6(d) is the Bode plot of the closed-loop system.

Fig. 7(a) shows two steps in  $x$  with the step size of  $10 \text{ nm}$ . The rms noise in steady state is within  $3 \text{ nm}$ . In Fig. 7(b), two steps of  $-4 \mu\text{m}$  and  $8 \mu\text{m}$  were generated at  $14.5$  and  $15.5 \text{ s}$ , respectively. The overshoot of the responses is  $3.25\%$ , and the settling time is within  $0.32 \text{ s}$ . Fig. 7(c) presents three steps of  $2 \mu\text{m}$  in  $z$ . The damping effect is clearly seen. This is due to the cables connected to the moving platen and the dc control effort to levitate the platen before the closed-loop-control motions are performed. Fig. 7(d) shows the smallest step size of  $0.1 \mu\text{rad}$  in the out-of-plane rotation. Three consecutive steps of  $0.1 \mu\text{rad}$  were performed in  $\theta_x$ . After the fourth step of  $-0.3 \mu\text{rad}$ , the platen moved back to the original angular position of  $-6.19 \times 10^{-5} \text{ rad}$ . Among the 6-DOF centimeter-

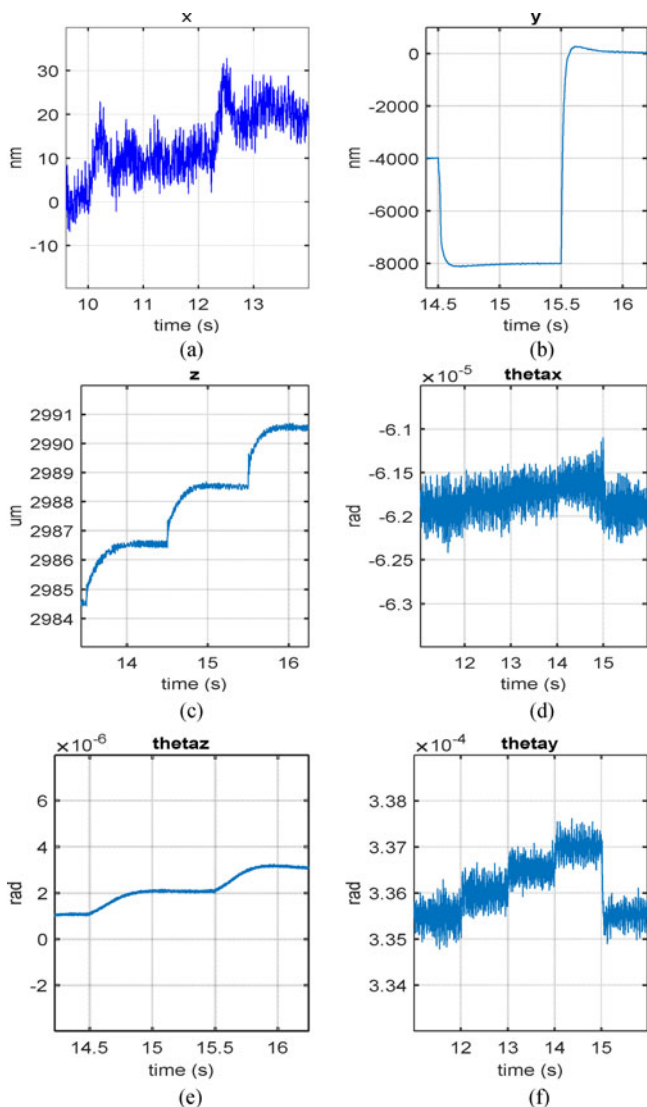


Fig. 7. Plots of step responses performed in each individual axis.

range nanopositioning stages, this is the best out-of-plane angular positioning resolution reported. Fig. 7(e) presents two consecutive steps of  $1 \mu\text{rad}$  in the rotation about the vertical axis. In Fig. 7(f), there are three steps of  $0.5 \mu\text{rad}$  and one step of  $-1.5 \mu\text{rad}$  in  $\theta_y$ .

Fig. 8 gives the positions of all six axes in magnetic levitation, where two circular motions with the diameter of 6 mm are performed in the  $xy$  plane. Right after the completion of the first circular motion, at 14 s, the maglev stage was paused for 0.125 s. The perturbations in  $\theta_z$ ,  $\theta_x$ ,  $\theta_y$ , and  $z$  are within 50, 290, 430, and  $20 \mu\text{m}$ , respectively.

The positioning precision reported above verifies the force calculation and the theoretical development of the 2-phase Lorentz-coil framework. The parameter identification is not to change the result of the force calculation. It just adds two more parameters to quantify the effects of the dc control effort and the external force disturbances. In (29),  $b_*(z_0)$ , the contribution of the force calculation in the system model, still stays in the augmented model.

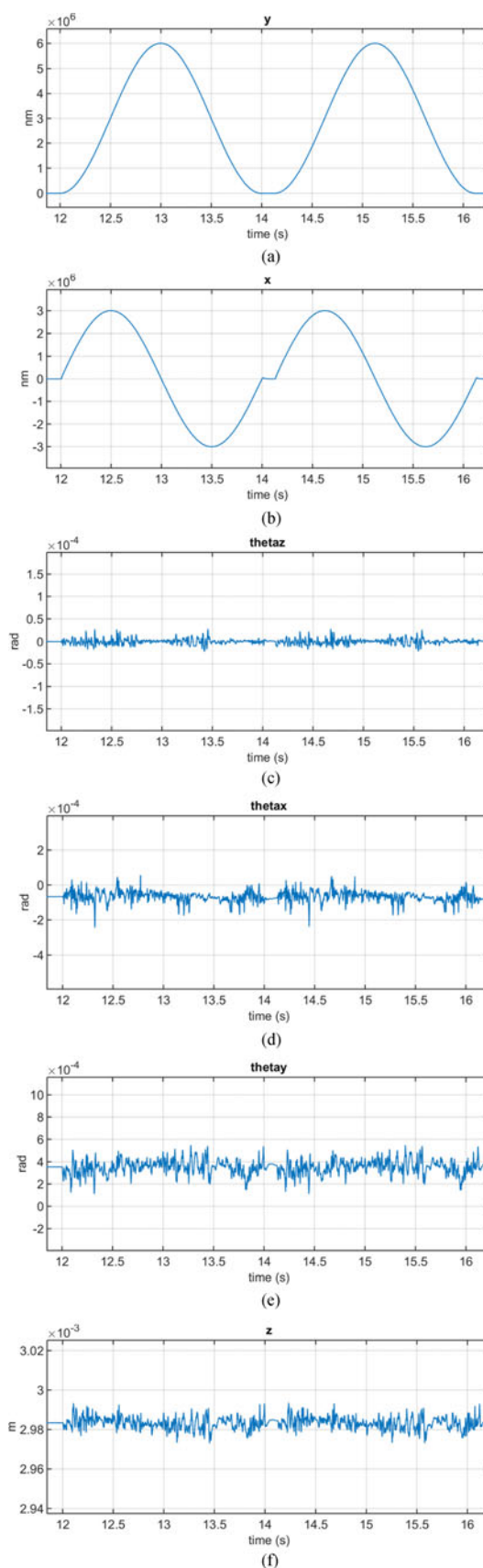


Fig. 8. Two circular motions with the diameter of 6 mm in the  $xy$  plane.

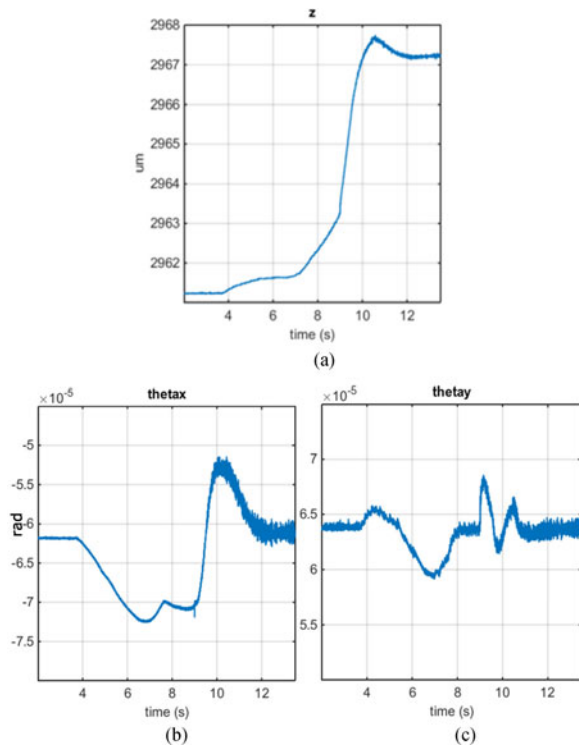


Fig. 9. Responses in a test with a load of 539.6 g added to the platen.

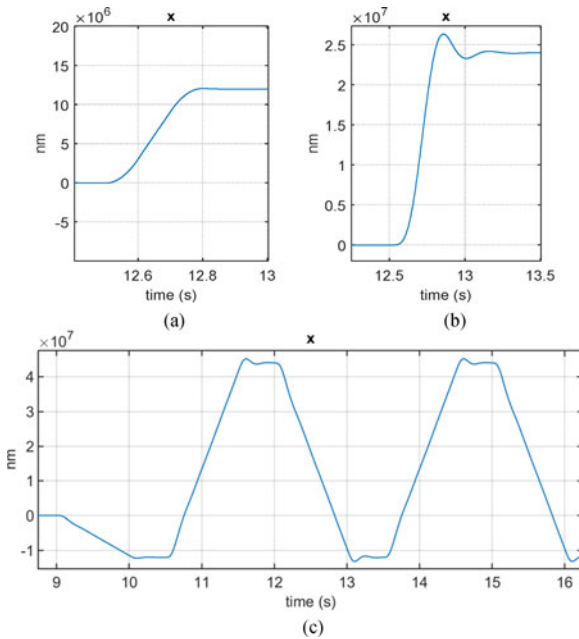


Fig. 10. The response in  $x$  to a trapezoidal-velocity input shaping with the displacement of (a) 12 mm, (b) 24 mm, and (c) 56 mm.

Fig. 9(a)–(c) shows the responses in  $z$ ,  $\theta_x$ , and  $\theta_y$  of an experiment in which a load of 539.6 g is added to the platen from the beginning with the same controllers. With the added mass, the errors of the system models in  $x$ ,  $y$ ,  $\theta_x$  and  $\theta_y$  are significantly larger. The peaks of the associated closed-loop transfer functions' gains are also larger. This results in the increased output noise when the loaded platen moves up in  $z$ . However, the closed-loop controllers effectively drive the out-of-plane angular positions,  $\theta_x$  and  $\theta_y$ , of the platen to the initial

set points. Fig. 10 is the motion in  $x$  in response to a trapezoidal-velocity input shaping. It is performed within 0.3 s with a travel distance of 12 mm. The velocity and acceleration are 60 mm/s and  $0.6 \text{ m/s}^2$ , respectively. Fig. 10(b) is the response to the same type of input shaping in the same time length, but the displacement is 24 mm. The achieved velocity and acceleration are 120 mm/s and  $1.2 \text{ m/s}^2$ , respectively. Fig. 10(c) shows the trapezoidal position profile of another translational motion with the displacement of 56 mm.

## VI. CONCLUSION

A universal framework with 2-phase planar Lorentz coils and a linear Halbach magnet array was developed and verified in this paper. The two orthogonal Lorentz forces generated by each 2-coil forcer are sinusoidally position-dependent in one horizontal axis. This framework allows for the force allocation of linear maglev motors and multiaxis stages. The framework was verified by a 6-axis maglev stage. Experimental results validated the force model and verified the reduced coupling between the forcers and that among the control axes. This 6-DOF stage is highly applicable in nanoprecision manipulation and assembly, stepping and scanning, and vibration isolation. This multiaxis stage is critically needed in applications, where both scanning and alignment are required concurrently. Targeted applications include precision stages for direct laser writing, stereo-lithography, and additive manufacturing of structures with the minimum feature size at the micro- and nanoscale. The framework presented herein can also be applied for moving-magnet motion-control stages with the dimension of the moving magnet array in the translational direction larger than that of the stationary coils to reduce the magnets' end effects.

## REFERENCES

- [1] W.-J. Kim, "High-precision planar magnetic levitation," Ph.D. dissertation, Dept. Elect. Eng. Comput. Sci., Mass. Inst. Technol., Cambridge, MA, USA, 1997.
- [2] T. Hu and W.-J. Kim, "Extended range six DOF high-precision positioner for wafer processing," *IEEE Trans. Mechatronics*, vol. 11, no. 6, pp. 682–689, Dec. 2006.
- [3] Q. Xu, "Design and development of a compact flexure-based XY precision positioning system with centimeter range," *IEEE Trans. Ind. Electron.*, vol. 61, no. 2, pp. 893–903, Feb. 2014.
- [4] Z. Zhang and C.-H. Menq, "Six-axis magnetic levitation and motion control," *IEEE Trans. Robot.*, vol. 23, no. 2, pp. 196–205, Apr. 2007.
- [5] C. M. M. van Lierop, "Magnetically levitated planar actuator with moving magnets: Dynamics, commutation and control design," Ph.D. dissertation, Eindhoven Univ. Technol., Eindhoven, The Netherlands, 2008.
- [6] C. Fulford and M. Maggiore, "Control of a 5DOF magnetically levitated positioning stage," *IEEE Trans. Control Syst. Technol.*, vol. 17, no. 4, pp. 844–852, Jul. 2009.
- [7] P. Berkelman and M. Dzadovsky, "Magnetic levitation over large translation and rotation ranges in all directions," *IEEE Trans. Mechatronics*, vol. 18, no. 1, pp. 44–52, Feb. 2013.
- [8] M. Mofushita, T. Azukizawa, S. Kanda, N. Tamura, and T. Yokoyama, "A new maglev system for magnetically levitated carrier system," *IEEE Trans. Veh. Technol.*, vol. 38, no. 4, pp. 230–236, Nov. 1989.
- [9] R. F. Post and D. D. Dyutov, "The inductrack: A simpler approach to magnetic levitation," *IEEE Trans. Appl. Supercond.*, vol. 10, no. 1, pp. 901–904, Mar. 2000.
- [10] P. J. C. Branco and J. A. Dente, "Design and experiment of a new maglev design using zero-field-cooled YBCO superconductors," *IEEE Trans. Ind. Electron.*, vol. 59, no. 11, pp. 4120–4127, Nov. 2012.
- [11] J. Jin and T. Higuchi, "Direct electrostatic levitation and propulsion," *IEEE Trans. Ind. Electron.*, vol. 44, no. 2, pp. 234–239, Apr. 1997.

- [12] M.-Y. Chen, M.-J. Wang, and L.-C. Fu, "Modeling and controller design of a maglev guiding system for application in precision positioning," *IEEE Trans. Ind. Electron.*, vol. 50, no. 3, pp. 493–506, Jun. 2003.
- [13] D. L. Trumper, M. E. Williams, and T. H. Nguyen, "Magnet arrays for synchronous machines," in *Proc. IEEE IAS 28th Annu. Meeting*, Oct. 1993, pp. 9–18.
- [14] H. Zhu, T. J. Teo, and C. K. Pang, "Design and modeling of a six-degree-of-freedom magnetically levitated positioner using square coils and 1-D Halbach arrays," *IEEE Trans. Ind. Electron.*, vol. 64, no. 1, pp. 440–450, Jan. 2017.
- [15] M.-Y. Chen, C.-F. Tsai, H.-H. Huang, and L.-C. Fu, "Integrated design of a planar maglev system for micro positioning," in *Proc. 2005 Amer. Control Conf.*, Jun. 2005, vol. 5, pp. 3066–3071.
- [16] S. Basovich, S. Arogeti, Y. Menaker, and Z. Brand, "Magnetically levitated six-DOF precision positioning stage with uncertain payload," *IEEE/ASME Trans. Mechatronics*, vol. 21, no. 2, pp. 660–673, Apr. 2016.
- [17] J. C. Compter, "Electro-dynamic planar motor," *Precis. Eng.*, vol. 28, no. 2, pp. 171–180, Apr. 2004.
- [18] V. H. Nguyen and W.-J. Kim, "A two-phase framework for linear permanent-magnet machines and multi-axis stages with magnetic levitation," in *Proc. 2014 ASME Dyn. Syst. Control Conf.*, Oct. 2014, Paper 5936.
- [19] V. H. Nguyen and W.-J. Kim, "Novel electromagnetic design for a precision planar positioner moving over a superimposed concentrated-field magnet matrix," *IEEE Trans. Energy Convers.*, vol. 27, no. 1, pp. 52–62, Mar. 2012.
- [20] V. H. Nguyen and W.-J. Kim, "Design and control of a compact light-weight planar positioner moving over a concentrated-field magnet matrix," *IEEE Trans. Mechatronics*, vol. 18, no. 3, pp. 1090–1099, Jun. 2013.



**Vu Huy Nguyen** (S'13–M'16) received the B.S. degree in mechanical engineering from the Hanoi University of Technology, Hanoi, Vietnam, in 2005, and the M.S. and Ph.D. degrees in mechanical engineering from Texas A&M University, College Station, TX, USA, in 2011 and 2015, respectively.

He is currently a Postdoctoral Research Staff Member with Lawrence Livermore National Laboratory, Livermore, CA, USA. His research interests include design, integration, and intelligent

control of mechatronic systems.



**Won-jong Kim** (S'89–M'97–SM'03) received the B.S. (*summa cum laude*) and M.S. degrees in control and instrumentation engineering from Seoul National University, Seoul, South Korea, in 1989 and 1991, respectively, and the Ph.D. degree in electrical engineering and computer science from the Massachusetts Institute of Technology, Cambridge, MA, USA, in 1997.

Since 2000, he has been with the Department of Mechanical Engineering, Texas A&M University College Station, TX, USA, where he is currently an Associate Professor and was the inaugural Holder of the Dietz Career Development Professorship II during 2007–2010. He is the holder of three U.S. patents on precision positioning systems. His current research interests include the analysis, design, and real-time control of mechatronic systems, networked control systems, and nanoscale engineering and technology.

Prof. Kim is fellow of the American Society for Mechanical Engineers (ASME) and a member of Pi Tau Sigma. He is or was the Technical Editor of the IEEE/ASME TRANSACTIONS ON MECHATRONICS; the *ASME Journal of Dynamic Systems, Measurement, and Control*; the *International Journal of Control, Automation, and Systems*; and the *Asian Journal of Control*.